8.1 Overview

The mechanical elements and services of the pixel detector are described in this section. We also describe the integration of the major components of the pixel detector and installation in ATLAS. The pixel detector, including the internal services, is located within the pixel support tube (PST) as already shown in Figure 2.1. A perspective view of the pixel detector elements within the PST is shown in Figure 1.

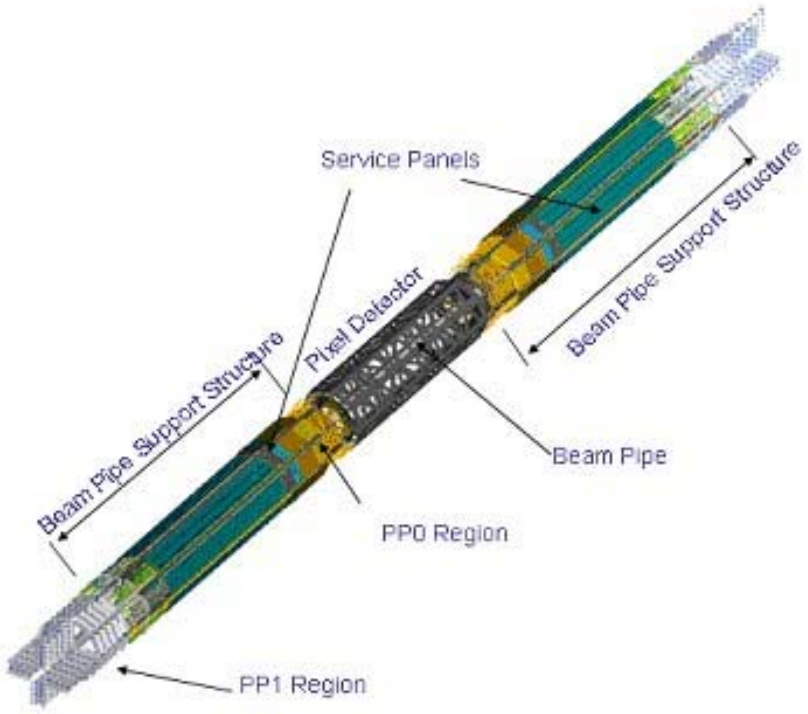

Figure 1: A perspective view of the active region of the pixel detector and of the internal pixel services and related support structures.

The active regions of the pixel detector are divided into a barrel region and two identical endcaps. The active elements in the barrel region are staves (with integrated cooling) each supporting 13 modules. The staves are held precisely by half-shells that are joined to form the three barrel layers of the detector. The active elements in the endcap regions are disk sectors (also with integrated cooling) each supporting six modules. Eight disk sectors are supported on a disk support ring. There are three disks in each of the two endcaps. The design and construction

of these barrel and endcap elements are described in subsequent sections of this chapter.

The barrel shells and the disk rings are rigidly supported by a support frame constructed in three sections a barrel section and two identical endcap sections. The support frame is constructed from carbon composites apart from small aluminum blocks in the regions where the barrel and endcap frame sections are bolted together. A picture of the support frame is shown in Figure 2. Four precision mounts are mounted on endplates attached to the support frame. These precision mounts engage mating supports in the PST when the support frame and the attached services slide through the PST during the installation procedure(section 7.7).

Figure 2: The support frame for the pixel detector.

The beryllium beam pipe [Ref] within the ATLAS detector is held on each side of the support frame by additional composite structures, the Beam Pipe Support Structure (BPSS). The BPSS also supports the Service Quarter Panels (SQP) that contain coolant pipes and all electrical services for the pixel modules [Section 6]. A low mass cable from each pixel module (Type 0 cable) is connected to the SQPs via small connectors at Patch Panel 0 (PP0 see Figure 1). The connections to the external services for the pixel detector are made to the SQPs at Patch Panel 1 (PP1) that is at the end of the Pixel Support Tube.

A schematic overview of the pixel electrical and optical services is given in Figure 3.

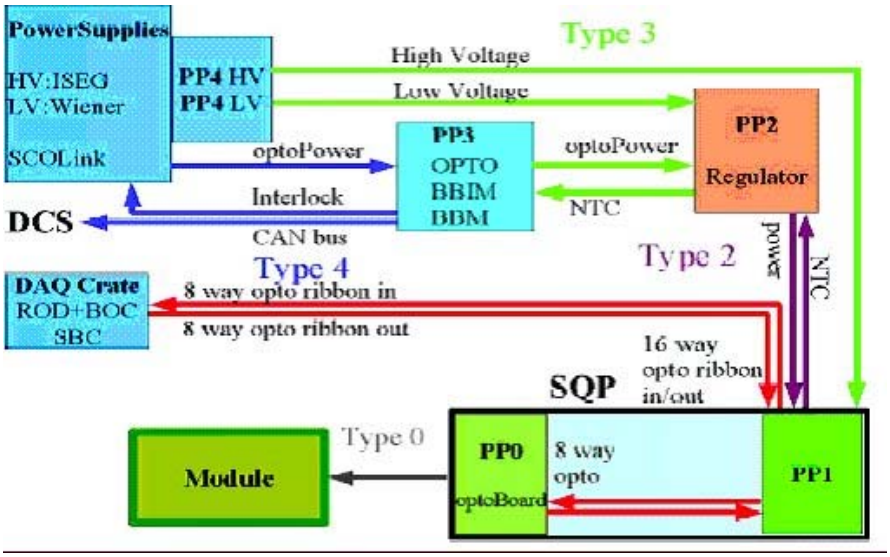

Figure 3: Schematic of the pixel electrical and optical services.

Optical transceivers (optoboards) are located on the SQPs (see Section 4.4 for a description of the optical system). Power for the pixel modules is supplied by power supplies located in the ATLAS services caverns [Ref] and is regulated at the Patch Panel 2 (PP2) location. High voltage is supplied by power supplies in the service caverns. Routing of low voltages and high voltages occurs at the Patch Panel 4 (PP4) region. Monitoring (and power distribution for the optical items) occurs at the Patch Panel 3 (PP3) region. Internal services (those within the Pixel Support Tube) are described in section 7.4. External services are described in section 7.5.

Cooling connections are also made at PP0 and at PP1. Individual heat exchangers for each pixel cooling circuit are embedded in the Service Quarter Panels. The heater exchangers and these connections are described briefly below in section 7.4. A general description of the ATLAS evaporative cooling system may be found in [Ref].

8.2 Barrel Region

The pixel detector barrel region (see Figure 4) has three concentric layers with modules loaded on local supports (staves) supported by three shells. The global support described in section surrounds the shells and supports them through four

radial fingers at the ends of the barrel region. Each stave [1] is about 800 mm long

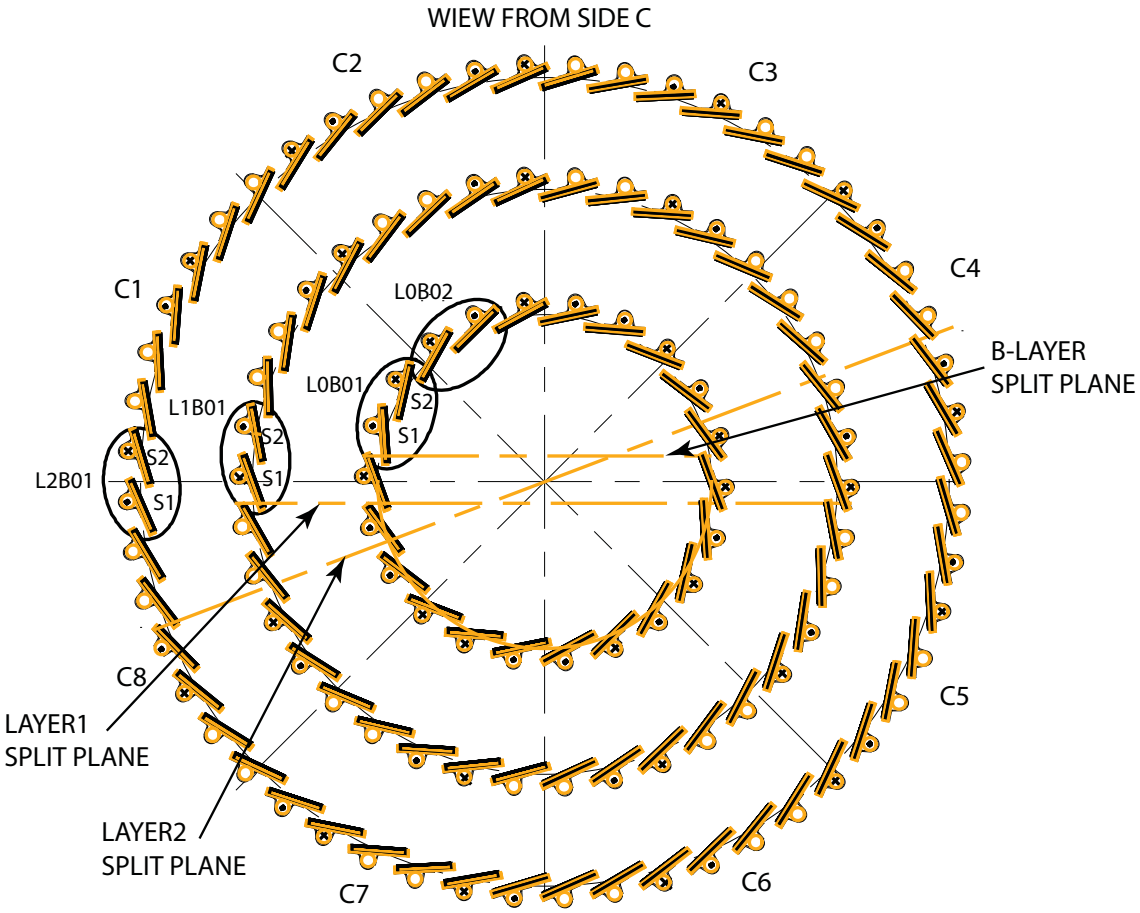

Figure 4: Layout of the Pixel barrel region. Support shells are not shown.

and carries 13 pixel modules tilted in both the Z-R and R-Φ planes by 1.1° and 20°, respectively. There are in total 112 staves. Two staves share a single cooling loop generating an assembly called a bi-stave with 26 modules. The modules are distributed over the three layers as summarised in Table 1.

8.2.1 Staves

A stave is an assembly of three parts (see Figure 5): a Thermal Management Tile (TMT); the omega piece; and the cooling pipe. The TMT is machined out of a Carbon-Carbon (C-C) plate yielding a series of 12 shingled steps symmetrically placed (6 each side) around a central flat step. The shingled geometry allows for

	B-layer	Layer 2	Layer 1	Total
Average radius [mm]	50.5	122.5	88.5	
No. of bi-staves	11	26	19	56
No. of staves	22	52	38	112
No. of modules	286	676	494	1456
No. of pixels	$1.317 \cdot 10^7$	$3.115 \cdot 10^7$	$2.276 \cdot 10^7$	$6.709 \cdot 10^7$

Table 1: Parameters of the pixel barrel region.

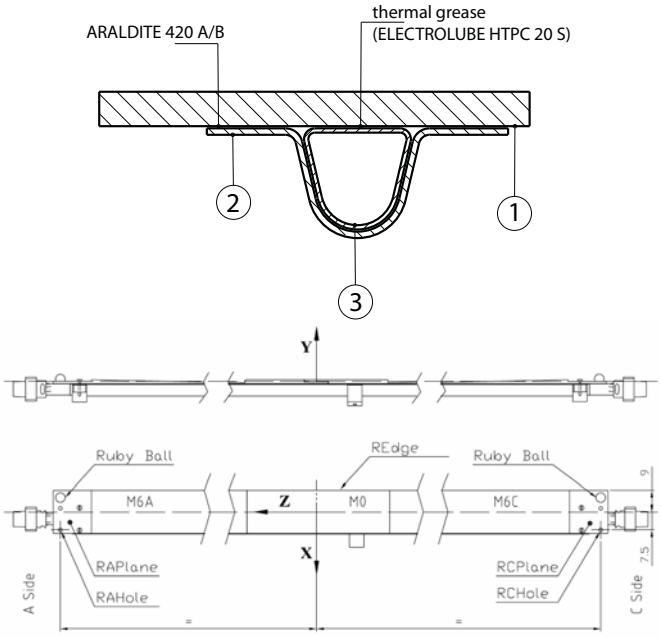

Figure 5: (a) top, cross section of a stave. Part 1 is the TMT, 2 is the omega piece and 3 the aluminum pipe. (b) bottom, longitudinal views of the stave with the reference system used for survey.

an overlap between the 13 modules mounted on the stave, to achieve hermetic coverage. The C-C material has been adopted for many reasons:

- good transverse thermal conductivity, adequate for an efficient heat transfer from the surface to the cooling channel;
- low radiation length;
- excellent stiffness and stability;
- low value (close to zero) of the coefficient of thermal expansion (CTE).

The omega piece is made of three layers of unidirectional, ultra-high modulus carbon fiber, with cyanate ester resin. The lay-up (0-90-0) is 0.3 mm thick and has been optimized through an extensive design and test program. The choice of the material and of the lay-up has been done in order to achieve a longitudinal CTE as close as possible to the CTE of the C-C TMT, to minimize distortions due to cool down of the structure. The omega-TMT-longitudinal CTE mismatch, less than 1 ppm, allows the stave to meet the stability requirements. The omega is bonded to the TMT using an adhesive[1)] featuring a high peeling strength.

A D-shaped (see part 3 in Figure 5) aluminum pipe, with a 0.3 mm thick wall, is located in the TMT/Omega structure. It provides the cooling channel for the C_3F_8 coolant. The aluminium tube is made of a 6061 Al-alloy, precisely shaped by extrusion to fit inside the omega piece with a clearance of 50 μm. The tube hydraulic diameter is 4.15 mm, which allows cooling of two staves in series with an acceptable pressure drop. A pressure drop of about 50 mbar over one stave has been measured during the thermal tests. Thermal grease[2)] is used to fill the gap between the tube and the TMT. Use of this grease interface reduces the mechanical coupling between the tube and the C-C. This minimizes the stave distortion from cool down.

During the production of staves, several problems were encountered that caused a change in the design and fabrication. The original design had the ends of the aluminium pipe coated with nickel, by an electroless process, in order to attach aluminium fittings by brazing. Staves, before and after modules were loaded, went through a qualification process that used an aqueous solution as a coolant. The presence of water triggered a corrosion process in the aluminium pipes. The corrosion was due to a galvanic process where water and traces of halogen (like Cl) acted as an electrolyte. The effect of the galvanic corrosion led in some cases to holes in the pipe, as may be seen in Figure 6.

[1)] CIBA Araldite® 420 A/B, from Huntsman, former Ciba Specialty Chemicals (www.huntsman.com)

[2)] HPGP thermal grease from Electrolube (www.electrolube.com).

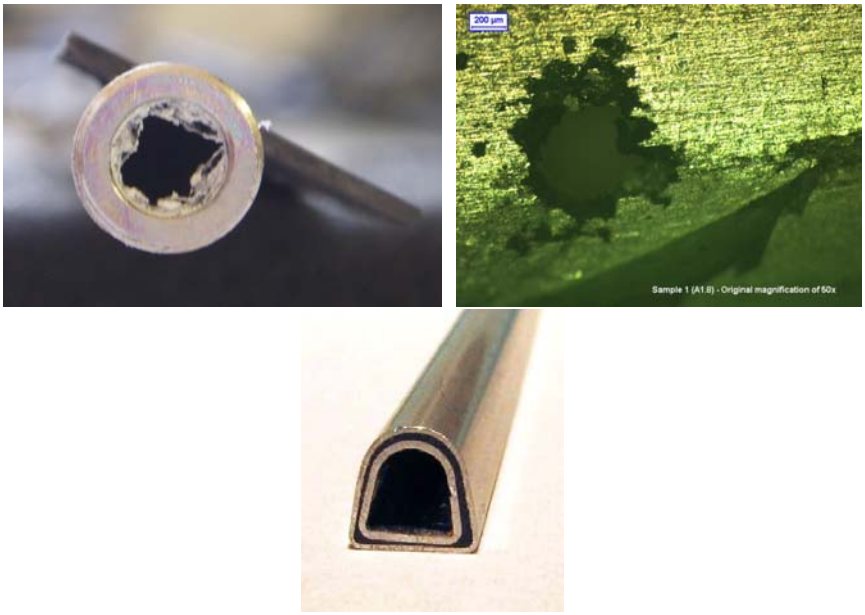

Figure 6: On the left, a view of the end of the stave pipe after corrosion. The nickel layer is detached from the aluminum by the formation of aluminum oxides. The picture in the centre shows a detail of the pipe with a through hole. On the right, a picture of an inserted pipe to recover staves already loaded with modules.

A significant number of staves had already been loaded with modules when this problem was found. The solution that was implemented was to insert a new pipe into the existing one. The inserted pipe (see Figure 6) a smaller hydraulic diameter that significantly increased the pressure drop along the pipe. Since the evaporation temperature depends on the pressure, there is a difference in the temperature (ΔT) between the first (higher T) and last (lower T) module of a stave, and this difference was increased for a smaller hydraulic diameter.

The thermal impedance from the coolant to the TMT is also increased for two pipes. There is a 150 μm gap between the two pipes, filled with an alumina loaded epoxy[3)] having a thermal conductivity of 1.1 W/mK. The ΔT increase is $\sim 4^{\circ}$C .

The new pipe was electrically insulated from the original one in order to protect against existing galvanic corrosion at the surface of the external pipe. Hard anodization with an oxide layer of about 30 μm of the inserted pipe was used.

The stave pipe was connected to a cooling system to verify the thermal properties. This connection applied forces to the stave pipe that were transferred to the omega piece, causing delamination the bond between the omega and the TMT. The bond quality was found to be poor because carbon powder from the C-C prevented good adhesion. The bond failure degraded significantly the thermal integrity of the grease layer between the pipe and the TMT. A dedicated inspection performed after the full production showed that more than 5 % of the staves were already delaminated at the fitting area and two of them where already loaded with modules.To prevent further delamination, a glass-filled PEEK collar was added to all the staves that were used in the detector.

The failure modes (corrosion and delamination) led us to develop a recovery plan for the staves already loaded with the modules and for the ones still to be loaded. The recovery plan from corrosion followed three different paths:

1. Insertion of a new aluminium D-shaped pipe into the corroded pipe. Tests performed with an evaporative cooling system have shown that modules of such bi-staves run above 0 $^{\circ}$C. Results are reported in Table 2.

2. Fitting were attached to all pipes by laser welding, thereby eliminating eliminating brazing.Bare staves (staves without modules loaded) were disassembled. The old pipe was removed and replaced with one with laser-welded fittings and reassembled with a yield of about 85%.

3. A new batch of staves was produced to compensate for the losses of the refurbished bare staves.

The barrel detector was assembled with a mixture of three different type staves. Table 3 shows how the stave types were assigned to the three layers

[3)] STYCAST 2850 FT from Emerson & Cuming (www.emersoncuming.com)

Bi-stave type	Stave type	Measured[4)]	
		Mean T	Max T
Repaired Bi-stave	Stave 1 (inserted)	$+3.3^\circ$ C	$+10^\circ$ C
	Stave 2 (clean)	-4.46° C	-0.5° C
Standard Bi-stave	Stave 1	-3.92° C	$+1^\circ$ C
	Stave 2	-5.61° C	0° C

Table 2: Estimated and measured temperature for different bi-staves. Stave 1 is upstream and Stave 2 is downstream in the cooling loop.

Type	Comments	Layer 2	Layer 1	B-Layer	Total
Inserted staves Pipe inserted (1)	26	0	0	26	
New Staves New pipes (2)	2	15	11	28	
Repaired Staves Pipe substituted (3)	24	23	11	58	

Table 3: Distribution of the different types of staves in the barrel layers.

8.2.2 Barrel Module Mounting

Modules mounting on staves started in the summer of 2004 to verify procedures. There were three module-loading sites. After qualification of all three sites, production continued at full speed until the corroded aluminum pipes in staves were discovered. This problem stopped module loading for six months. Once new staves were available, module loading was immediately restarted and later continued in parallel with bare stave production. The last stave was assembled in October 2007.

The loading procedure and the qualification tests are described in the following paragraphs. Stave loading was done using specially designed robots in a semi-automatic way by trained operators. Three module loading robots were installed: sites 1 and 2 had similar designs (shown in Figure 7), while site 3 had a different one [2]. All setups were located in clean rooms with temperature control.

Detector modules had to be fixed with a precision better than $50\,\mu$m in both directions on the stave plane. Nominal module positions were defined in a stave reference coordinate system constructed individually for each stave based on stave reference points (machined edges, tile steps and reference planes on stave ends). Some of these reference points are inaccessible after stave loading, so to control the module positions and to translate these positions to the global ATLAS coordinate frame, two precision ruby balls were mounted on each stave. Together with the reference planes, they allow the measurement of module positions.

The determination of the stave reference frame and the survey of module positions after stave loading was done with a coordinate measuring machine (CMM)

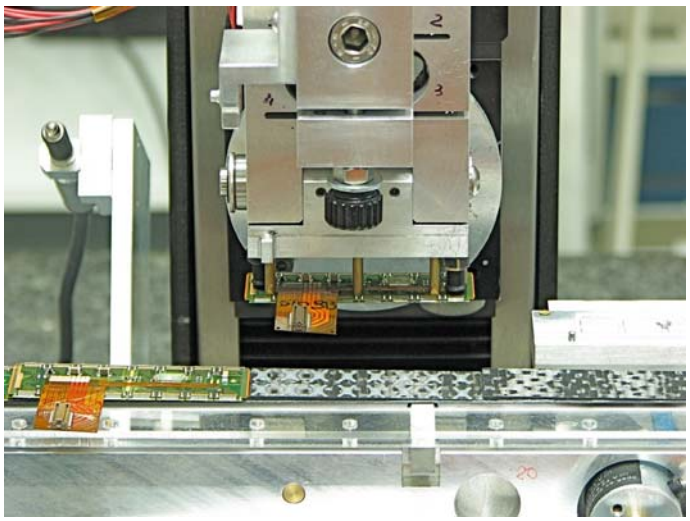

Figure 7: Loading robot used in sites 1 and 2. Blow up of the module pick-up head.

with mechanical, optical and laser probes at sites 1 and 2. Site 3 used a specially designed optical system connected with the loading robot. The single point measurement precision was between 5 and 10 μm for contact probes and between 5 and 20 μm for optical probes depending on the surface quality. Several measured points were averaged to improve accuracy.

Loading started with a determination of the stave reference system. The stave was fixed on a moving trolley (sites 1 and 2) or granite table (site 3) to guarantee precise placement of the modules by the loading robot. To guarantee uniform cooling, a gap between a pixel module and the stave surface must be constant ($\sim$100 μm) everywhere. Due to the shingled-stave design, modules are inclined by $\sim$1.10° before gluing. The ideal position of a pixel module located 100 μm above the stave surface was stored in the robot memory and module was moved away to allow glue deposition.

A thermal-conducting, flexible epoxy glue [5)] was used to fix modules. After glue deposition, a module was returned by the robot to its predefined position 100 μm above stave surface and left in this position until the glue cured. The force holding the module was adjusted to control the quality of module-stave joint.

A loaded stave was surveyed on a CMM. Deformation of pixel modules (bow) was measured using different methods. All measurements were taken with respect to the two ruby balls mounted on each stave. The deviation of modules position from nominal in X (transverse to the stave axis) and Z (along the stave axis) co-

[5)] Toray Silicone SE4445CV A&B, from Dow Corning (www.dowcorning.com)

ordinates are shown in Figure 8 [3]. Only a few modules have deviations bigger than 50 μm.

The fully-loaded staves under to measure a characterization procedure to test the modules after the loading as well as to measure the thermal performance of the assembly. The testing sequence was similar to the one used to qualify modules individually. The testing sequence was as follows:

- module configuration, measurement of threshold dispersion and noise, threshold scan without bias to check for disconnected pixels and a sensor bias I-V scan to check the integrity of the sensor at room temperature;
- ten thermal cycles between -30°C and 30°C with a cycle time of 2 hours;
- the same tests as performed at room temperature but at about -8°C with the addition of a radioactive-source scan for the identification of disconnected pixels. The thermal performance was also obtained.

A ranking function of the measured parameters was constructed to determine the stave quality and to select the staves for a particular layer. The best staves went into the B-layer. Staves with an inserted pipe were only used in Layer 2 (Table 2).

8.2.3 Half-shells

The barrel shells (see Figure 9) were constructed from two half-shells. Bi-staves were attached to a half-shell. Ten aluminium-alloy fasteners screw each bi-stave to support rings bonded to a shell. All the shells are supported off the end-cones of the pixel support frame (Section 8.l) PEEK elements are bonded at both ends of the half-shell to provide the interface to the fingers of the end-cones. Shells were made from carbon-fiber-reinforced material. A quasi-isotropic laminate made of six plies $(0^\circ/60^\circ/-60^\circ)$ of unidirectional ultra-high-modulus carbon fiber[6)]/cyanate-ester[7)] was made. The shells are not cylinders, but have flat surfaces locally. The overall mass was reduced by cutting out material in each shell, as show in Figure 9.

The accuracy of the interface to a stave was set to be better than 50 μm. The maximum gravity deflection of each assembly was designed to be less than 50 μm. Table 4 shows results from a survey done on the as-built assembly. The values reported in the table are the maximum deviations observed over several hundred data points taken all over the structures. The large majority of them ($> 90\%$) are within the specifications.

[6)] Carbon fiber YS80, from Nippon Graphite Fiber Corporation (NGF) (http://www31.ocn.ne.jp/ ngf/english/)

[7)] EX-1515 Cyanate Ester resin system, from TenCate Advanced Composites, former Bryte Technologies Inc (www.brytetech.com)

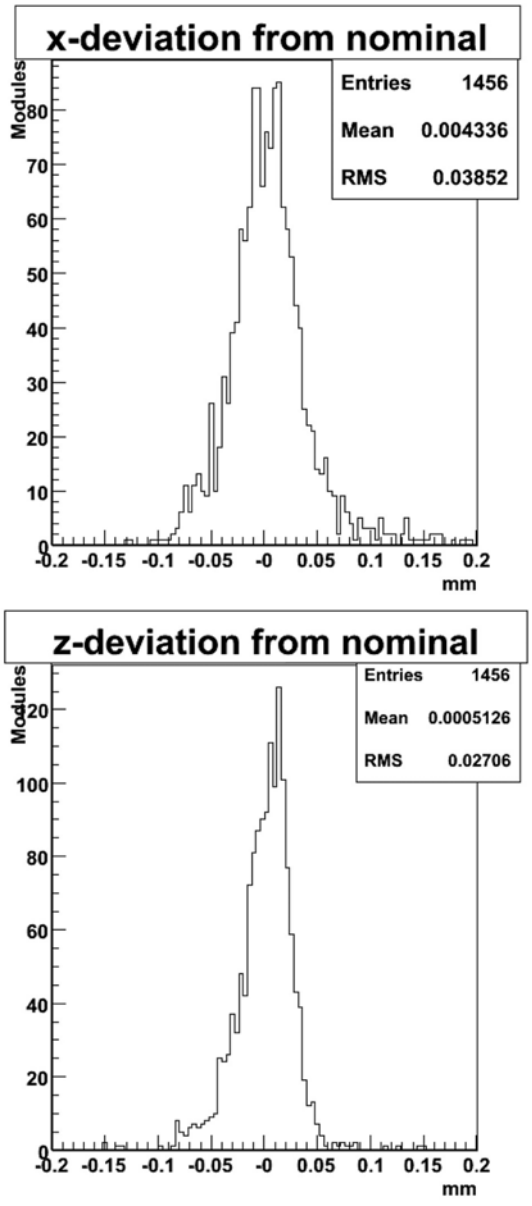

Figure 8: Deviation of module positions from nominal values for the barrel modules as described in the text.

Figure 9: Picture of the three barrel shells

	Shell Accuracy [μm]			
	Requirements	As built		
	All Layers	Layer 2	Layer 1	B-Layer
Geometrical accuracy	50	70	62	55
Gravity sag	50	98	68	80

Table 4: Comparison between the geometrical design requirements and the maximum deviations from an ideal geometry as surveyed.

8.2.4 Bi-stave Integration and Half-shell Loading

Two staves (see Figure 10), each loaded with 13 pixel modules, were assembled together. Type 0 cables (section 8.5) were connected to the module and properly routed along the staves. Electrical testing was done during bi-stave assembly as was leak checking of the two cooling loops after connection of a U-link (section 8.5)

Figure 10: A bi-stave assembly.

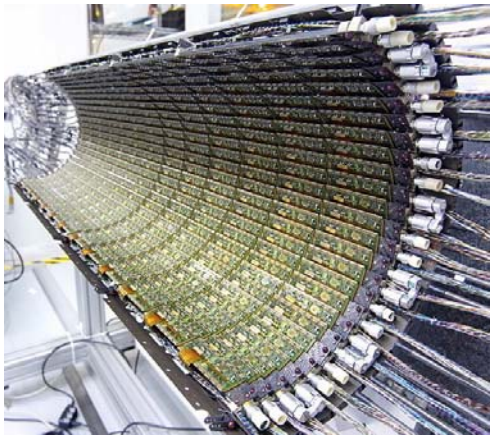

Figure 11: Layer 2 half-shells with all the bi-staves installed.

Bi-staves were integrated by hand into the half-shells starting with Layer 2 and proceeding to the B-Layer. Figure 11 shows one of two half-shells with all the bi-staves installed for Layer 2.

Once the bi-stave loading was completed, the half-shells underwent a geometrical survey. The stave reference points provided by two ruby balls glued at the ends of each stave were surveyed with respect to the half-shell reference points. Although the module position is known in Z with a typical accuracy of about 10 μm, the inaccuracy in Φ and in R is significantly worse. The stave can bow in a half-shell during attachment up to 200 μm in Φ at the central support (Z=0). The effects on individual modules could not be determined because modules could not be surveyed directly on a half-shell.

8.2.5 Half-shell Clamping

Two half-shells of each layer were clamped together into a complete shell. A half-shell lacks torsional stiffness (around the axis of the cylinder). Half-shells were stiffened with an external structure and kept undeformed during the integration process. The shell transferring tool (STT) held each of the two half-shells by ten clamps that grabbed each half-ring in two places. The tool was placed on the flat surface of a granite table that provided the reference plane. The bottom half-shell is kept on the STT and the top one was lowered until it engaged the clamping features (see Figure 12).

The operation was delicate due to the fact that the wire bonds of the modules were exposed and clearances were about 1mm. Once the half-shells are joined, they can be removed from the STT. The load of the shell was taken by the metal pipe passing through the shell and visible in Figure 12. Figure 13 shows the Layer 2 shell clamped and moved onto the integration and testing tool (ITT) for integration into the global support frame (section 8.6). Layer 1 followed the same clamping procedure. The B-layer required a more complex procedure. The flanges at the extremities of the beam pipe do not pass through the B-Layer and it has to be clamped around them (Section 8.6). More details of the assembly and testing procedures can be found in [4].

8.3 Endcap Region [Version of November 23, 2007]

The active elements of the pixel detector in the two endcap regions are disk sectors, each supporting six modules (three on each side). Eight disk sectors are supported on a disk support ring, forming a disk. There are three disks in each of the two endcaps. The disks in the endcaps are rigidly held by a support frame constructed from carbon composites. This section will describe the construction, survey and testing of the disk sectors (8.3.1), disks (8.3.2) and endcaps (8.3.3).

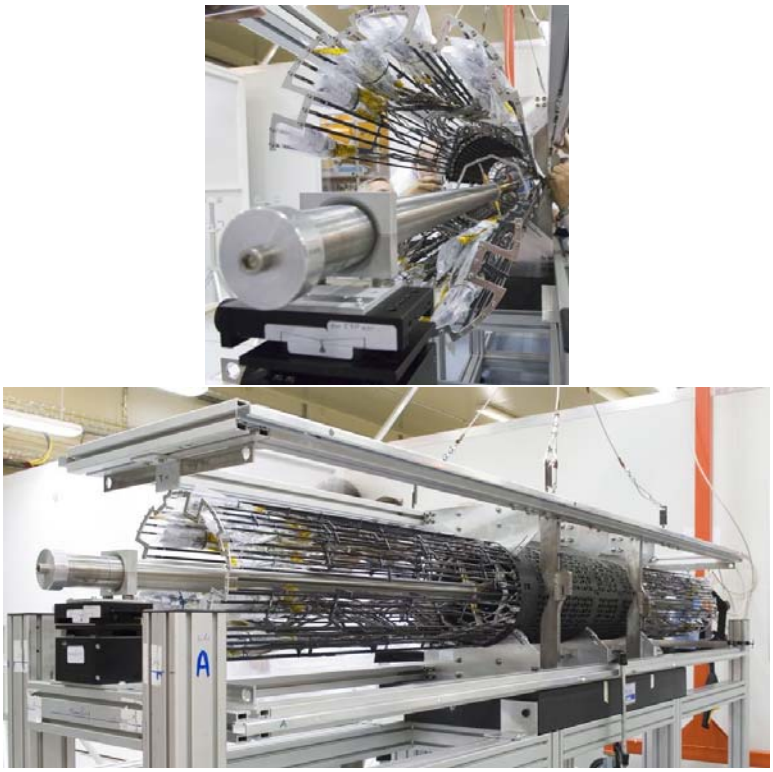

Figure 12: Clamping of the Layer 2 half-shells. The top half is craned onto the bottom one resting on the STT (see text). The picture shows the mechanism that guides the process. The stainless steel pipe, visible along the the axis of the shell, was used to guide the insertion into the global frame and was removed afterward.

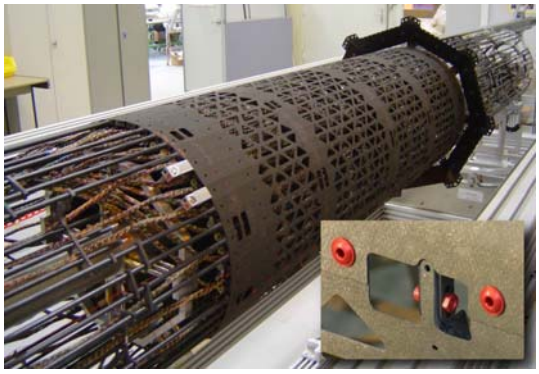

Figure 13: Layer 2 clamped and resting on the axis of the ITT before being inserted into the global frame.

8.3.1 Disk Sectors

8.3.1.1 Construction

The local support structures (with integrated cooling) for the modules in the endcap region are called disk sectors. The sectors are roughly trapezoidal in shape, and consist of two thin carbon composite sheets with a rectangular aluminum cooling tube and carbon foam in between the sheets. The cooling tube is bent into a W-like shape to fit within the sector, and makes contact with the carbon composite sheets with a compliant, thermally conducting adhesive. Each cooling circuit in the disk region serves two sectors.

[Text here from Gil on the physical construction of the sectors.]

Three modules are mounted on each side of the sector, with the long dimension of the module in the radial direction. The three modules on the back of the sector are rotated 7.5 degrees with respect to the modules on the front side, thus providing full overlapping azimuthal coverage. Figure 14 shows three modules mounted on the front side of a sector.

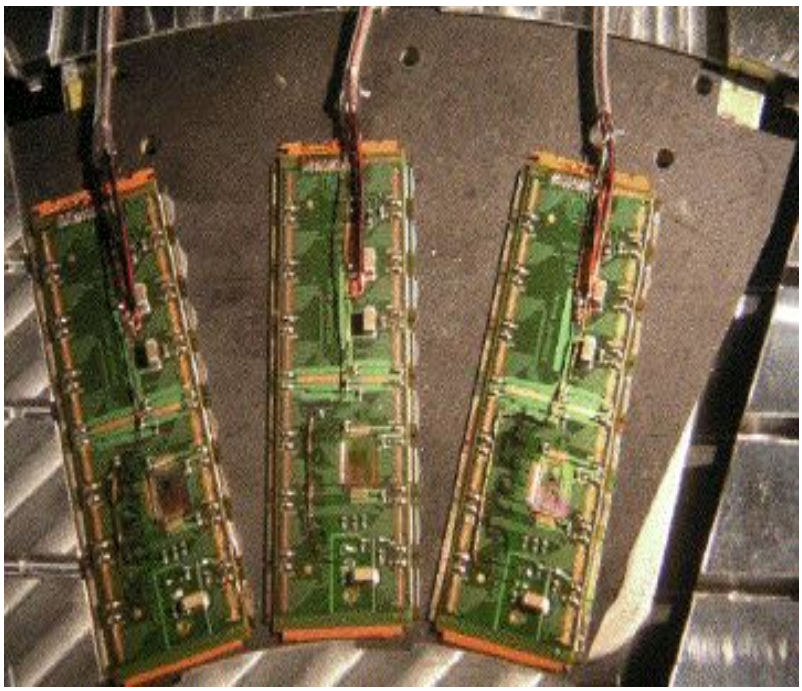

Figure 14: Three endcap pixel modules mounted on the front side of a sector.

The modules are glued to the sectors with Dow Corning silicone SE4445. Nylon filaments of 110 μm diameter are used to control the silicone thickness.

During the gluing operation the position of survey targets in the corners of each module are viewed with an optical SmartScope, to ensure that the modules are placed in the correct positions on the disk sectors. The modules are positioned and glued on each sector with a precision of 2 μm in the plane of the module and about 10 μm perpendicular to the module plane.

8.3.1.2 Sector Survey

After the modules are glued to the carbon surface of the disk sectors, the sector is again mounted on the table of an optical SmartScope. The SmartScope very precisely measures X,Y coordinates (in the plane of the sector) by measuring the position of the table, and measures Z coordinates (perpendicular to the sector) with optical focusing. The SmartScope is used to measure the X,Y position of survey targets at the 4 corners of modules mounted on a disk sector, and these measurements are used to determine the position and orientation of the module in the plane of the sector. The SmartScope also measures 32 X,Y,Z points on the top side of modules mounted on a sector (16 along one long edge, 16 along the other long edge) in the vicinity of the first and last chip ID pads of each front-end chip, and these measurements are used to determine the position and rotations of the module out of the sector plane. The pixel module is treated as a flat rigid plane, as the module distortions (such as bow) are very small.

From the above SmartScope measurements the alignment parameters of each module were calculated in the local module reference frame. The module alignment parameters are those 6 parameters used to describe a flat plane: X, Y, Z, Φ_x, Φ_y, Φ_z. X is the coordinate across the short width of the module, and Y is the coordinate along the long length of the module. In the local module reference frame the module alignment parameters are the displacements of the module from its nominal position (i.e. the difference from nominal). The X,Y,Φ_z alignment parameters calculated from the sector surveys are not the final survey alignment parameters, as they do not include the effect of the placement of the sector on the disk ring. Details about the calculation of the module alignment parameters are given in [5].

In Figure 15 are the distributions of the X,Y,Φ_z module alignment parameters calculated from the sector surveys (treating all the modules as A Disk modules, which means plotting the negative of the actual X and Φ_z values for the C Disk modules), and in Table 5 are the means and sigmas of the Gaussian fits to these distributions. One sees several features:

- The mean of the X alignment parameter distribution is different for front and back modules: -2.8 μm for front modules, and $+2.8$ μm for back

modules. This is due to a small systematic offset when the modules were mounted on the sectors. The opposite sign occurs when converting the survey measurements to the same coordinate system.

- The average sigma for the X and Y alignment parameter distributions is 2.0 μm, and the sigma for the Φ_z alignment parameter distribution is 0.064 mrad. These resolutions include both the placement accuracy and the measurement precision, and thus represent upper limits on the placement accuracy. These small values show that the modules have been placed on the sectors with excellent accuracy of better than 2 μm.

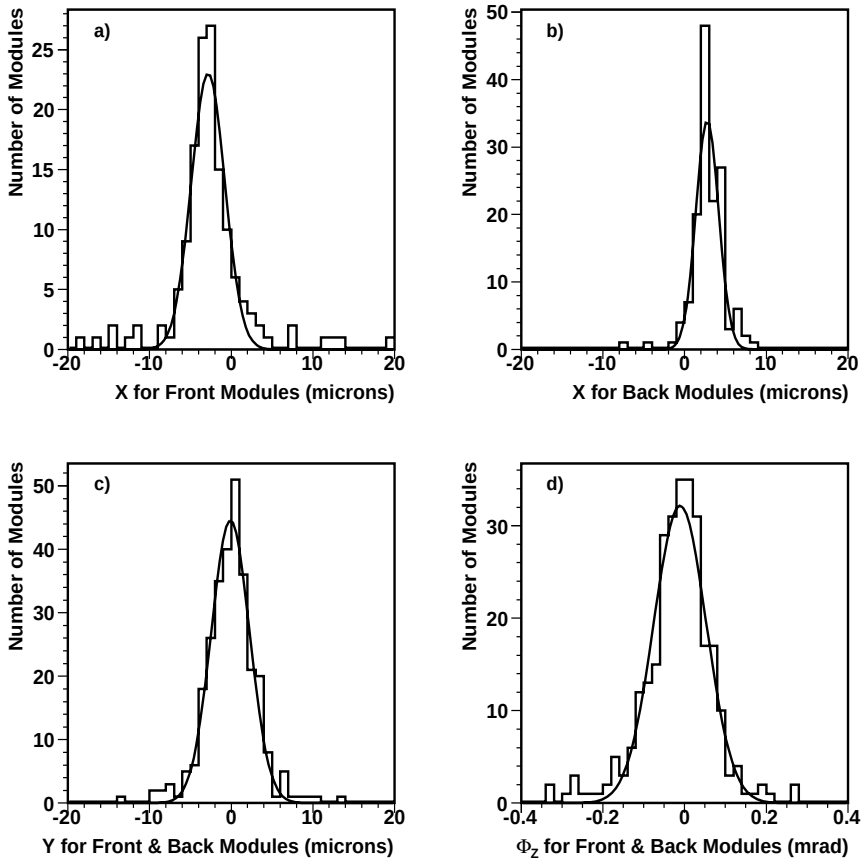

Figure 15: X,Y,Φ_z alignment parameters calculated from the sector surveys.

8.3.1.3 Sector Testing

	Mean	Sigma
X for Front Modules	-2.8 ± 0.2 μm	2.1 ± 0.2 μm
X for Back Modules	$+2.8 \pm 0.1$ μm	1.4 ± 0.1 μm
Y for Front and Back Modules	-0.1 ± 0.1 μm	2.3 ± 0.1 μm
Φ_z for Front and Back Modules	-0.011 ± 0.004 mrad	0.064 ± 0.004 mrad

Table 5: Results of the Gaussian fits to the sector survey distributions in Figure 15.

Electrical and thermal tests are performed on the modules after they are glued onto the sectors. The goal is to check any degradation of module performances (early breakdown, increased noise, bump failures, etc.) caused by thermal or mechanical stresses from loading. Another aim is to rank the sectors for disk loading so that the sectors with the least number of bad pixels can be loaded onto the innermost disks. The tests performed on each module are part of the full quality control procedure of the ATLAS Pixel Detector and more details are given in [6]. The electrical sector testing sequence consists of the following three sets of basic monitoring scans:

- LOAD test: This test is performed immediately after sector loading at room temperature. The test includes I-V, digital, analog threshold, crosstalk and source scans. Data from this test are compared to the single module BURN test (a test performed under similar conditions before the module was loaded on the sector) to observe any changes due to sector loading. All six modules on the sector are tested individually before proceeding to the next test.

- INBURN test: During this test the sector is cold soaked for a period of about 12 hours at -30°C with the power off. It is then thermal cycled between -20°C and 20°C (T_{NTC}=-16 to 25°C) with the power on. The dwell time at each endpoint is 1 hour and the entire test consists of 14 cycles with about 3.5 hours per cycle. Digital and analog threshold scans are run throughout the burn-in, while monitoring T_{NTC} and digital/analog voltages and currents.

- STAVE test: The full electrical characterization is performed after burn-in at operating temperature (T_{NTC}= -5 to -10°C) for a fully configured module. The test includes all LOAD scans as well as MonLeak, in-time threshold and GDAC scans. Data from this test are compared to the single module FLEX test to detect any changes due to sector loading or sector burn-in, and serve as the basis for sector ranking.

Electrical testing and burn-in were performed using one setup. The details of the technical description are given in [7]. The standard module testing hardware chain was used: a PC computer with VME and GPIB interfaces (control cards), ATLAS Pixel TurboDAQ software, a VME crate with a custom board (ATLAS Turbo Pixel Low Level card), an external custom board (ATLAS Turbo Pixel Control Card), GPIB controlled off-the-shelf power supplies, and a LBNL custom designed SURF board with module(s) attached to it. Two surf boards [8] were used to connect all six modules at once. The sector was cooled using an inert flourocarbon C_6F_{14} running in a secondary loop connected to the sector cooling pipes. Dynalene (HC-50) was used in the primary loop and was cooled using a chiller. The two loops made thermal contact inside a coiled heat exchanger.

The following measurements made during the electrical tests described above were used to rank the sectors: bias current at 150 V, number of bad pixels in digital scans, number of bad pixels in analog threshold scans, number of bad pixels in crosstalk scans, number of bad pixels in in-time scans, number of bad pixels due to bump discontinuity, number of dead or masked pixels measured during source scans, threshold dispersion, and average noise.

The cuts for bad pixels are defined according to guidelines from the ATLAS Pixel Detector collaboration. The above quantities were entered into the Pixel DataBase to maintain a comlete record of the production sequence and allow the possiblity of tracing any eventual problems. Sector evaluation also considered results from the alignment survey and thermal performance measurements during the electrical tests.

The total number of bad pixels in each of the endcaps can be estimated using the results of the STAVE test performed at the sector level since this is the last, full electrical characterization performed on the modules at operating temperature. It is also the last source scan where bump discontinuity can be accurately measured. Table 6 shows the total number of bad pixels for each of the endcaps, classified by failure. Bad pixels are not double counted: if a pixel is bad digitally, it is not counted as analog bad or source bad.

EndCap	SOURCE	MASK	DIG	ANA	DISC	XTALK	INTIME	TOTAL	%
A	5497	373	5816	471	2559	171	2671	17531	0.26
C	4221	360	52	594	636	127	3131	9036	0.14

Table 6: *Number of bad pixels for each endcap, classified by failure. Results are taken from the STAVE test and later connectivity tests.*

8.3.2 Endcap Disks

8.3.2.1 Construction

Eight disk sectors are mounted on a 312 mm diameter carbon composite disk support ring, forming a disk. There are three disks in each of the two Endcaps. Each disk has 48 modules, for a total of 288 modules. The radius of the module centers is approximately 119 mm. The inner radius of the active area of the pixel modules is approximately 89 mm. Figure 16 shows one of the completed disks.

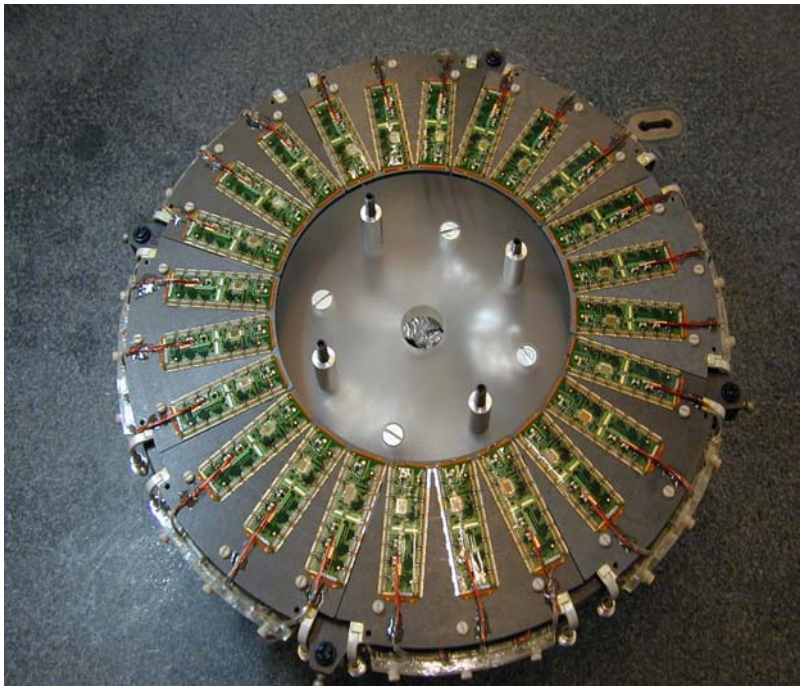

Figure 16: Eight sectors assembled into a disk.

8.3.2.2 Disk Survey

After the disk sectors are mounted on the disk ring, the X,Y positions of the survey targets at the four corners of each front module are again precisely measured with the SmartScope, and are used to determine the final survey position and orientation of the front modules on the disk with a precision of a micron. The back modules are not surveyed after mounting the sectors on the disk, but the measurements done after mounting the modules on the sectors are used to calculate the positions of the back modules on the disks with a precision of about 5 microns.

The final X,Y,Φ_z alignment parameters of the modules were calculated from the disk survey SmartScope measurements in a manner similar to the way they

were previously calculated for the sector survey measurements. These final X,Y,Φ_z alignment parameters are the displacements from nominal due to both the placement of the modules on the sector and the placement of the sectors on the disk ring.

In Figure 17 are the distributions of the final X,Y,Φ_z module alignment parameters calculated from the disk surveys (treating all the modules as A Disk modules, which means plotting the negative of the actual X and Φ_z values for the C Disk modules), and in Table 7 are the means and sigmas of the Gaussian fits to these distributions. One sees several features:

- The average sigma for the X and Y alignment parameter distributions is 12 μm, and the sigma for the Φ_z alignment parameter distribution is 0.130 mrad. These values include both the placement of the modules on the sector and the placement of the sectors on the disk ring. Recall from the sector survey results (which only include the placement of the modules on the sector), that the average sigma for X and Y was 2.0 μm, and the sigma for Φ_z was 0.064 mrad. Thus we see a much larger variation in the module position due to the sectors being placed on the disk ring than due to the modules being placed on the sector.

- The mean of the Y alignment parameter distribution is 35 μm. The local module Y direction is the radial direction in the disk. The reason that the Y alignment parameter is so large is mostly because the average radius of the mounting holes in the disk rings is larger than the nominal value of 156 mm. From independent disk ring measurements, the radius appears to be roughly 25 μm larger than nominal. This accounts for the major part of the 35 μm.

	Mean	Sigma
X for Front Modules	-0.1 ± 1.1 μm	12.6 ± 0.9 μm
X for Back Modules	1.1 ± 1.0 μm	11.5 ± 0.8 μm
Y for Front and Back Modules	35.3 ± 0.7 μm	11.4 ± 0.6 μm
Φ_z for Front and Back Modules	-0.029 ± 0.008 mrad	0.130 ± 0.009 mrad

Table 7: Results of the Gaussian fits to the disk survey distributions in Figure 17.

8.3.2.3 Disk Testing

After the sectors were mounted on a disk ring, a continuity test was performed on the modules. Its purpose was to quickly check that the delicate module circuitry

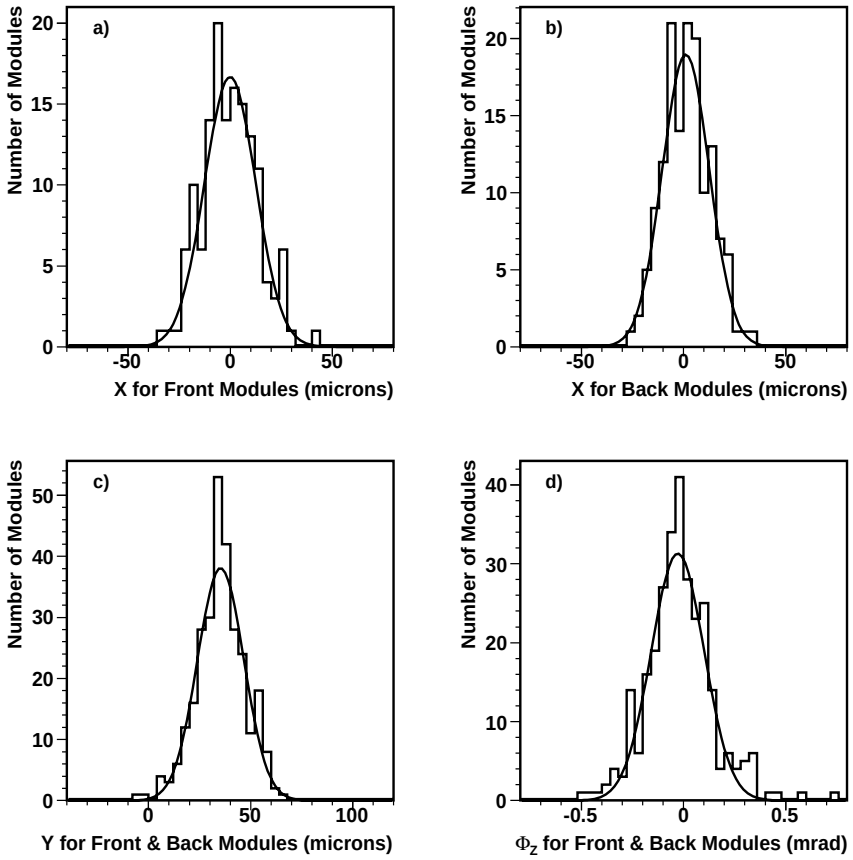

Figure 17: Final X,Y,Φ_z alignment parameters calculated from the disk surveys.

survived the mounting operation and any sector or disk handling. Since it was done without cooling, at room temperature, the modules were powered on a chip-by-chip basis, one-at-a-time, and only for a short time. The continuity test was performed as each sector was mounted on the disk ring, and again upon the disk completion. It took about 5-10 minutes per sector.

An electrical test was then done after the continuity test. The purpose of the electrical test was to check that no subtle changes occurred during the mounting of the sectors on the disk ring, and to verify the stable performance of all modules. The electrical test was a shorter version of the LOAD test done during sector testing, and it involved the following scans:

- MCC scan: This is a test of the MCC operation and connectivity.

- Digital functionality: This scan checks all registers (global and pixel front-end) and all buffers using digital injection to test full overflow conditions. It tests all pixels with digital injection (digital inject scan). This must do be done with nominal VDD voltage at 40 Mbps single link, 80 Mbps single link, 40 Mbps dual link, and 80 Mbps dual link.

- Analog functionality: This is the most time-consuming and complex set of scans performed with the bias voltage on. It is a sequence of operations and scans needed to certify proper analog behavior: threshold tune using internal injection to set a uniform threshold along the module, internal injection threshold scan (measures threshold and noise of each pixel using internal injection), FDAC tune and test, ToT tuning (tune the ToT response to a MIP signal for each pixel in order to have a uniform response to the collected charge in a time acceptable for operation in ATLAS; it calibrates the relationship between the measured ToT and collected charge), and the cross-talk scan to measure the cross-talk fraction and to detect bump defects resulting in increased capacitive coupling between pixels.

- Noise occupancy: This test consists of enabling one front-end chip at a time in self-trigger mode and measuring the rate of hits. Whereas pixels that generate hits at a rate greater than 1 Hz (1 kHz) are flagged as hot and are disabled in the slow (fast) mask during module and sector testing, it is not the case during disk testing. Here we only record their total number and compare these results with noise scans performed during sector testing.

A sensor bias voltage measurement was performed after the electrical scan was finished because we could not control the relevant power supply from the ATLAS TurboDAQ program. The bias voltage was ramped up to 600 V in 10 V increments to check for possible sensor damage. The current stability at different bias voltages was investigated over a period of more than 15 minutes.

8.3.3 Assembly of Disks into Endcaps

8.3.3.1 Construction

To assemble each endcap, three disks were rigidly supported by four mounts within a lightweight, octagonal, carbon composite support frame, shown in Figure 18.

Figure 19 shows a perspective cut-away view of the pixel detector. The view shows individual barrel and endcap modules, supported with their associated services on staves and disks within the octagonal support frame.

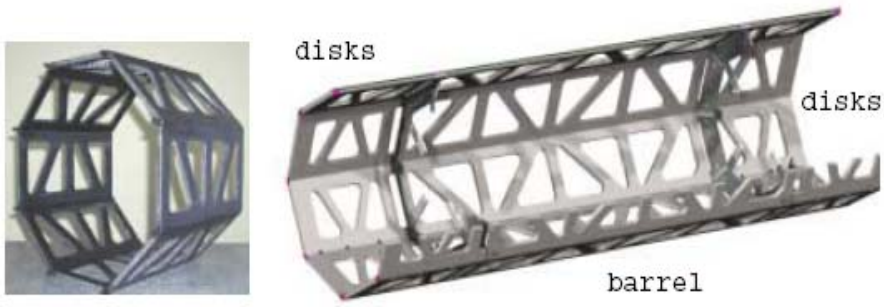

Figure 18: Carbon composite support frames.

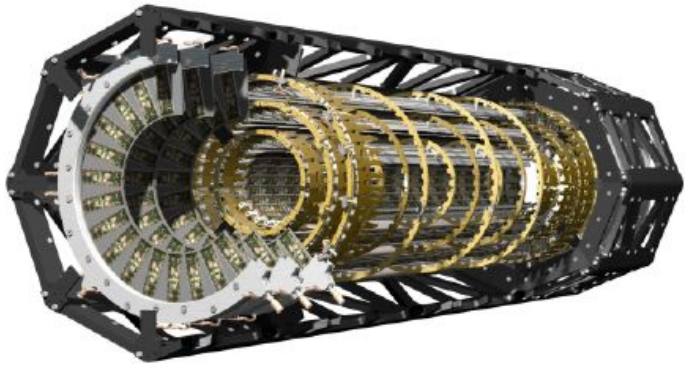

Figure 19: A perspective cut-away view of the pixel detector..

8.3.3.2 Endcap Survey

No surveys were done of the modules or sectors after the disks were assembled into an endcap, since the relevant fiducial marks were not viewable at that point.

8.3.3.3 Endcap Testing

All cooling circuits on both endcaps were leak checked down to $1-4 \times 10^{-9}$ Torr. This is the value required by the evaporative cooling system.

A connectivity test of the endcaps was performed at various stages of the integration to ensure that no modules were damaged during handling or transport. A connectivity test consists of a series of basic functionality checks performed chip-by-chip with no cooling. Each module is powered briefly and the digital, analog and bias voltages and currents are measured and compared to a set of standard values. A MCC scan is then performed as well as FE chip register/receiver tests.

Each FE chip is configured to measure voltages and currents, which are compared to expected values. Finally, a short threshold scan is performed with and without bias voltage to verify that the high voltage is properly delivered to the module. The total testing time required for one endcap is two days.

A connectivity test was performed on both endcaps after loading, but before shipment to CERN.

The connectivity test was repeated after delivery of the endcaps to CERN to verify that no modules were damaged during the transport. Testing of Endcap C at CERN showed no failures on any of the modules. Endcap A showed no failures at CERN other than the three failures reported before shipment. An additional connectivity test for Endcap C was performed after integration into the Pixel Package. The test found one module with missing high voltage due to a weak bond on the module. The bond was repaired by adding silver epoxy to the high voltage hole.

Since Endcap A was used in a system test at CERN, an additional connectivity test was performed before any further integration to check for any damage to the modules during the system test or during handling in preparation for the system test. There were several modules found with intemittent HV failures. These problems were fixed by re-soldering the HV pins on the ELCO connector, by adding solder to HV wire connections, by adding silver epoxy to HV bonds, or by reinforcing glue tacks.

References

[1] M. Olcese, C. Caso, G. Castiglioni, R. Cereseto, S. Cuneo, M. Dameri, C. Gemme, K. W. Glitza, G. Lenzen, and F. Mora. Ultra-light and stable composite structure to support and cool the atlas pixel detector barrel electronics modules. *Nucl. Instr. and Meth. A*, 518(3):728–737, 2004.

[2] Karl-Heinz Becks, Peter Gerlach, Karl-Walter Glitza, Pascal Knebel, Peter Mattig, Bernd Sanny, Sebastian Reuschel, Swetlana Springer, and Bernd Witt. Local support assembly of the atlas pixel detector. *Nucl. Instr. and Meth. A*, 565(1):102–105, 2006.

[3] A. Andreazza, V. Kostyukhin, and Madaras. R. Survey of the atlas pixel detector components. ATL-IP-QC-0035, CERN, Sept. 2006.

[4] E. Andersen, K. Einsweiler, D. Giugni, C. Glitza, G. Lenzen, N. Hartman, M. Garcia-Sciveres, M. Gilchriese, M. Olcese, L. Rossi, B. Sanny, E. Vigeolas, and S. Coelli. Atlas pixel detector assembly and testing of the pixel detector system. ATL-IP-QA-0007, CERN, October 2007.

[5] A. Andreazza, V. Kostyukhin and R. Madaras, *Survey of the ATLAS Pixel Detector Components*, ATL-IP-QC-0035 (2007).

[6] ATLAS Pixel Collaboration, *ATLAS Pixel Module Electrical Test Description*, ATL-IP-QP-0144 (2004).

[7] ATLAS Pixel Collaboration, *Pixel Module Test Setup Specifications*, ATL-IP-ES-0088 (2003).

[8] ATLAS Pixel Collab., *http://pixdata.lbl.gov/surf/ambush/doc/surf-html/index.html*